Article

Crystallization of Fe-W-B Amorphous Powder Prepared by Gas Atomization

Shuwang Ma [1,*], Zheng Lv [1], Jian Wang [1], Haicheng Wang [1], Jian Yang [1,2], Zhimin Yang [1,2], Jingli Li [3] and Zhiyong Xue [3]

1   Advanced Electronic Materials Institute, GRIMAT Engineering Institute Co., Ltd., Beijing 101407, China
2   State Key Laboratory of Advanced Materials for Smart Sensing, GRINM Group Co., Ltd., Beijing 100088, China
3   Institute for Advanced Materials, North China Electric Power University, Beijing 102206, China
*   Correspondence: mashuwang@grinm.com; Tel./Fax: +86-010-60662603

Abstract: In this work, the effects of master alloy composition and annealing temperature on the amorphization and crystallization behavior of Fe-W-B powders prepared by gas atomization using compacts of Fe, W and B powder mixture were systematically studied. The results show that only the master alloy with high content of W (19.9 at.%) and B (13.6 at.%) of the six alloys studied yielded amorphous Fe-W-B powders. The alloying elements W and B are believed to have a glass-forming ability (GFA)-enhancing effect, which together with the high cooling rate of gas atomization leads to the formation of amorphization. The difference in the average particle size of 3–10 μm for the six atomized powders indicates that the master alloys with different W and B contents have different superheat and melt viscosity at the same atomization temperature. The Fe-W-B amorphous powder is structurally stable within 600 °C and crystallizes from the edge of the particles when the temperature increases to 700 °C, and its crystalline precipitates include α-Fe, FeWB and Fe_7W_6. The nuclear shielding tests and Monte Carlo N Particle Transport Code (MCNP) calculated results revealed that the Fe-W-B amorphous powder has a much better shielding performance for γ-rays and neutrons than that of iron. This work provides an efficient strategy for fabricating Fe-W-B amorphous powder with promising nuclear shielding potential and sheds light on the crystallization behaviors of this alloy.

Keywords: amorphous powder; gas atomization; crystallization; shielding performance

1. Introduction

Fe-W-B system materials have many special physical and chemical properties, which can be used in many promising potential applications, such as nuclear shielding, microwires, corrosion-resistant coating and wear resistant materials [1,2].

In recent years, several studies have been carried out on Fe-W-B-based alloys with the consideration of function–structure integration [3–6]. However, the high contents of intermetallics or borides (such as Fe_7W_6, FeWB, Fe_xB and W_xB_y) within crystalline Fe-W-B alloys, which is due to the phase transitions by continuous cooling from the liquid state, restrict the mechanical properties and corrosion resistance [7–10]. Elaborated Metallic glass can be prepared by various techniques, such as mechanical alloying, atomization and chemical methods. An amorphous $Al_{50}(Fe_2B)_{30}Nb_{20}$ powder mixture was prepared by mechanical alloying in a high-energy planetary ball-mill under argon atmosphere [11].

Metallic glasses have unique combinations of mechanical properties, corrosion resistance and magnetic property due to their non-crystalline structure. In recent years, more and more studies have focused on metallic glass, such as amorphous nanocrystalline powder, amorphous strips and so on [12–16]. A kind of amorphous Fe-W-B nano-powder was obtained via a chemical method [17]; nevertheless, the low yield makes it difficult to realize mass production.

Therefore, it is necessary to find a way to reduce the cost and simplify the manufacturing process. One of the technologies of rapid-solidification is gas atomization, which is used to produce metal powder [18–20]. By comparison, gas atomization is commonly used in the production of alloy powder by large-scale industry. This technique consists of breaking a liquid metal stream into droplets using a high-velocity flow. These droplets become powder particles after solidification. The droplet size is small, usually in the micron range. The particle size of the atomized powder usually ranges from a few microns to tens of microns.

Up to now, many Fe-B-based amorphous alloy powders have been successfully prepared by gas atomization [21–24]. However, atomized Fe-W-B amorphous powder with high content of W and B has not been prepared and studied to the best of our knowledge.

In this study, several types of Fe-W-B powder were prepared using the gas atomization method. The influence of alloy composition on the phase structure of the powder was investigated. It is important to remark that the powder with amorphous and crystalline structures was obtained successively after atomization and subsequent annealing treatment. To reveal the crystallization behavior of Fe-W-B amorphous powder, the influence of annealing temperature on phase transformation and thermal characteristics was investigated. The γ-ray- and neutron-shielding properties of Fe-W-B amorphous powder were calculated to evaluate its nuclear shielding performance.

2. Materials and Methods

2.1. Preparation of Powder

The precursors for the gas atomization are compacts of Fe, W and B powder mixture. The purity of Fe, W and B powders were 99.9 wt%, 99.9 wt% and 99.5 wt% and the FSSS particle sizes of Fe, W and B powders were 6 μm, 3 μm and 2 μm, respectively. Commercial elemental Fe, W, and B were weighted to give the required six compositions of master alloys as shown in Table 1. Tungsten content increases gradually from Sample 1 to Sample 6. All samples can be divided into two series. The tungsten content of Series 1 (Sample 1 to Sample 3) is less than 36 wt.% and Series 2 (Sample 4 to Sample 6) is higher, which is more than 44 wt.%. Generally, the liquidus temperature of the master alloy, which mainly varies with the content of tungsten and boron, is closely related to the atomization process.

Table 1. Compositions of Fe-W-B master alloys used in this work.

Serial Number	Sample Number	Compositions of Master Alloys			
		Percentage	Elements		
			Fe	W	B
Series 1	Sample 1	Mass (wt.%)	81.3	18	0.7
		Atomic (at.%)	89.9	6.1	4
	Sample 2	Mass (wt.%)	71.4	25.8	2.8
		Atomic (at.%)	76	8.4	15.6
	Sample 3	Mass (wt.%)	61.9	35.6	2.5
		Atomic (at.%)	72.5	12.7	14.9
Series 2	Sample 4	Mass (wt.%)	53.7	44.2	2.1
		Atomic (at.%)	68.7	17.2	14.1
	Sample 5	Mass (wt.%)	54.5	44.8	0.7
		Atomic (at.%)	75.9	19	5.2
	Sample 6	Mass (wt.%)	49.4	48.6	2
		Atomic (at.%)	66.4	19.9	13.6

The elemental mixtures of Fe, W and B were alloyed by vacuum induction melting. Each ingot was re-melted at least three times for homogeneity. Atomization was performed in an industrial-scale supersonic gas atomizer with nitrogen as the atomizing gas. The alloy was melted in a magnesia crucible utilizing a medium-frequency induction furnace under a nitrogen atmosphere. The alloy was heated to 1700 °C and a homogenization time of about 10 min was adopted. The value of the atomization gas pressure was 4.0 MPa. The melt droplets were quenched in the atomization and cooled down to room temperature in the collecting chamber. The residence time of atomization was about 1~2 minutes.

2.2. Performance Testing Method

The structures of the Fe-W-B powder were examined by X-ray diffraction (XRD, X'Pert PRO MPD from PANalytical, Westborough, MA, US) with Cu K_α radiation, in the 2θ range from 10° to 90°, in steps of 0.02° and at a scanning rate of 5°/min. The crystallized phases were identified by using the Crystallographica Search-Match (CSM) X-ray diffraction phase analysis software. The crystallization temperature (T_x) of Fe-W-B powder annealed at different temperatures was measured by differential scanning calorimetry (DSC, Netzsch STA 449 F3 from NETZSCH-Gerätebau GmbH, Selb, Germany) at a heating rate of 10.0 K/min under flowing high purity argon. The microstructures of Fe-W-B powder were carried out using scanning electron microscopy (SEM, JSM-6700F from JEOL, Tokyo, Japan) and transmission electron microscopy (TEM, FEI Tenai G2 F20 from Thermo Fisher Scientific, Waltham, MA, US). Selected area electron diffraction (SAED, FEI Tenai G2 F20 from Thermo Fisher Scientific, Waltham, US) was also utilized to identify the phase and crystal structure of Fe-W-B powder.

3. Results and Discussion

3.1. Effect of Alloy Composition on the Morphology and Structure of Gas Atomized Fe-W-B Powder

3.1.1. Morphology and Microstructure Analysis

The morphology of atomized powder with various compositions is shown in Figure 1. It can be observed that most of the particles are nearly spherical, but a few are irregular in shape. The irregular particles might be ascribed to the adhering aggregation of the melted droplets caused by an unsuitable air flow rate in the atomization process. In the condition of very high air flow, the speed of spheroidization is less than solidification. Thus, when the droplets have completed solidification, spheroidization has not been completed in time.
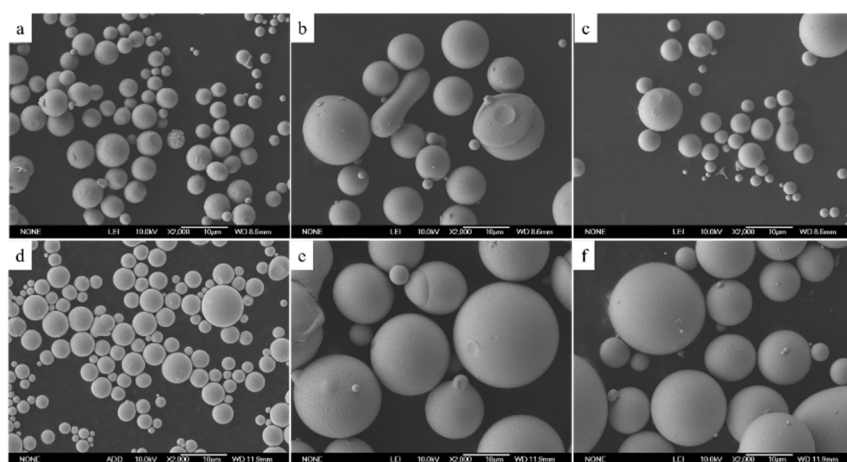

Figure 1. Morphology of atomized powder obtained at 1700 °C with different compositions (SEM).(**a**) Sample 1; (**b**) Sample 2; (**c**) Sample 3; (**d**) Sample 4; (**e**) Sample 5; (**f**) Sample 6.

It can also be seen that the particle size of the powders from sample 1 to sample 4 is small, with an average particle size of 3–7 µm, while the particle size of the powders for sample 5 and sample 6 is larger, with an average particle size of 9–10 µm. The average

particle size of the atomized powder is directly proportional to the viscosity and surface tension, both of which are related to the superheat of the molten master alloy.

The relationship between the viscosity coefficient and the temperature is given as follows [25]:

$$\eta = Ae^{\frac{E}{K_B T}} \tag{1}$$

where E is the activation energy, A is the constant, K_B is the Boltzmann constant, T is the absolute temperature and η is the viscosity coefficient. The higher the melting temperature, the lower the viscosity.

The relationship between the surface tension and the temperature is given as follows [26]:

$$\sigma_m \left(\frac{M}{\rho_m} \right)^{-2/3} = K(T_C - T) \tag{2}$$

where σ_m is the surface tension, ρ_m is the density, M is the molar mass of the metal melt, T_C is the critical temperature and K is the experimental constant. The higher the melting temperature, the lower the surface tension.

For Series 1 (Sample 1 to Sample 3), the master alloy with low tungsten content has lower liquidus temperature (T_l), which relates to higher superheat and lower melt viscosity at the same atomization temperature. Under this condition, it is easy to prepare fine powder. For Series 2 (Sample 4 to Sample 6), the master alloy with high tungsten content has higher T_l than that of Series 1. Higher tungsten content will increase the T_l of the master alloy, while a higher boron content will reduce it. Sample 4 has a lower tungsten content (17.2 at.%) and a higher boron content (14.1 at.%) than sample 5 and sample 6. Thus, Sample 4 should have higher superheat and lower melt viscosity than sample 5 and sample 6 at the same atomization temperature, which leads to the smaller particle size (average particle size of 4 μm) of Sample 4 and the larger particle size (average particle size of 9–10 μm) of Sample 5 and Sample 6.

Figure 2 shows that the microstructures of the particles with various compositions are quite different. The microstructure of Sample 6 is relatively uniform, and there is no obvious precipitated phase structure within the particle. For other types of particles, there are more or less precipitated phase structures, showing bright blocks or dendritic.
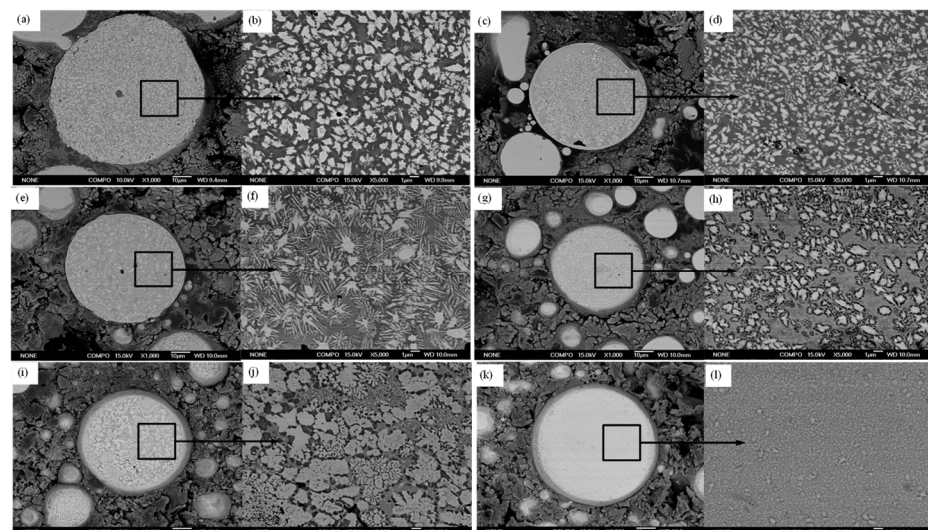

Figure 2. Microstructure of the particles with different compositions (SEM). (**a**,**b**) Sample 1; (**c**,**d**) Sample 2; (**e**,**f**) Sample 3; (**g**,**h**) Sample 4; (**i**,**j**) Sample 5; (**k**,**l**) Sample 6.

3.1.2. Phase Analysis

XRD patterns of atomized powder with various compositions at room temperature are shown in Figure 3. The XRD pattern of Sample 6 displays a broad peak between 35°

and 55°, indicating the existence of particles with an amorphous character. It reveals that only Sample 6 shows an amorphous phase (named as Fe-W-B amorphous phase), while other types of powder show crystallized phases or the coexistence of an amorphous phase and crystalline phase. The crystallized phases mainly contain α-Fe or mix with a small number of $W_xFe_yB_z$-type phases, such as FeWB and Fe_7W_6.
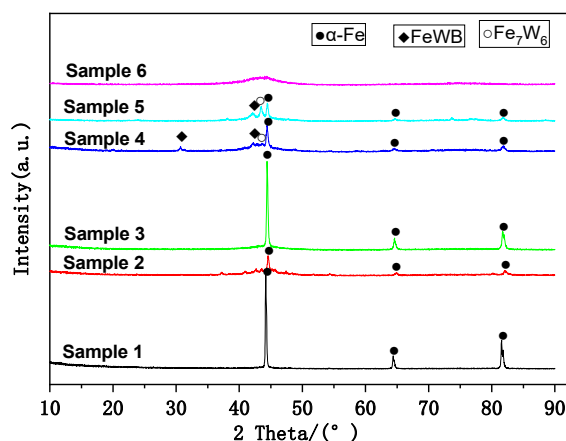

Figure 3. XRD patterns of atomized powder with different compositions at room temperature.

Regarding the successful preparation of Sample 6 amorphous powder, we believe that the intrinsic mechanisms involved include two main aspects. The first is related to the high cooling rate of the gas atomization. It is known that in the most usual method of amorphization, the high cooling rate should be applied to form an undercooled liquid or a metallic glass. The small size of the droplets, typically in the micron range, and the high velocity of the gas enable a fast heat transfer; in this way, it is possible to achieve very high cooling rates during the gas atomization.

Secondly, glass-forming ability (GFA) is very crucial for understanding the origins of glass formation. It has been indicated that any alloying element added to the finemet composition means that the GFA increases and crystallization transformation is delayed [27]. T_x/T_l is a reasonable indication of GFA based on the crystallization process of an undercooled liquid. The system with a larger T_x/T_l ratio could have a higher GFA [28]. In this study, the addition of tungsten and boron to the iron melt increased GFA and delayed the crystallization transformation, which promoted the formation of amorphization. Generally, an alloy with the composition of deep eutectics has a high GFA [29]. The master alloy of Sample 6 with higher tungsten and boron content is close to the composition of deep eutectic region, where the four-phase invariant reaction is conducted at 1365 °C: eutectic types, L$\Leftrightarrow$ μ+WFeB+α-Fe [30]. Furthermore, the addition of a high melting point W into Fe-B system will tend to increase the crystallization temperature. Thus, the Fe-W-B system of Sample 6 has a higher crystallization temperature (T_x) and lower liquidus temperature (T_l) at once. Therefore, Sample 6 should have higher GFA than other samples, which makes it show an amorphous phase only.

3.2. Thermal Characteristics and Crystallization Behavior of the Fe-W-B Amorphous Powder

Information concerning the structure change with temperature is quite important for the physical properties of amorphous material. To further study the stability of the amorphous structures of the Fe-W-B powder, the annealing treatment at different temperatures was designed for Sample 6. Therefore, several kinds of powder were annealed in vacuum at different temperatures ranging from 100 °C to 1000 °C for 1 h, respectively.

As shown in Figure 4, the amorphous structures of the Fe-W-B powder remain even as the temperature reaches 600 °C, which indicates that the amorphous structures are stable. When the temperature reaches 700 °C, it begins to generate a small number of α-Fe and Fe_7W_6 phases while the amorphous phase still exists. When the temperature reaches 800 °C

or 1000 °C higher, all amorphous phases are transformed into crystalline phases, which are mainly composed of α-Fe, FeWB and Fe_7W_6.
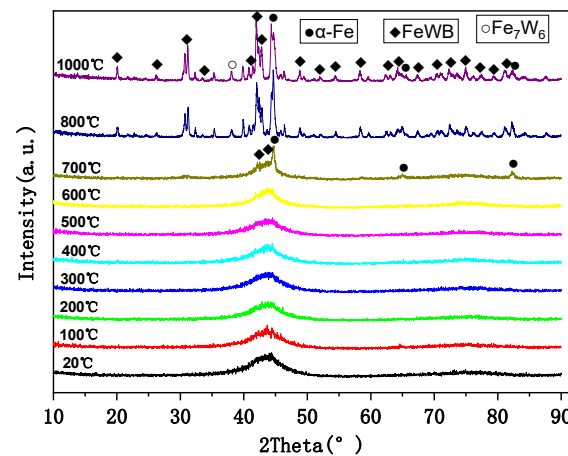

Figure 4. XRD patterns of FeWB amorphous powder processed by annealing at different temperatures.

The thermal stability of Fe-W-B amorphous powder was investigated by DSC, and the DSC curves of as-atomized and annealed Fe-W-B amorphous powder are shown in Figure 5. The DSC traces exhibit exothermic reactions corresponding to the crystallization of Fe-W-B amorphous powder as atomized. It shows a two-step process for the crystallization of amorphous structure. The first crystallization temperature (T_{x1}) of Fe-W-B amorphous powder is determined to be 607.73 °C, and the second crystallization temperature (T_{x2}) is determined to be 805.01 °C. After annealing at 800 °C or 1000 °C, the DSC curves show no exothermic reactions because Fe-W-B amorphous powder has completed the crystallization process, which is also consistent with the previous XRD analysis.
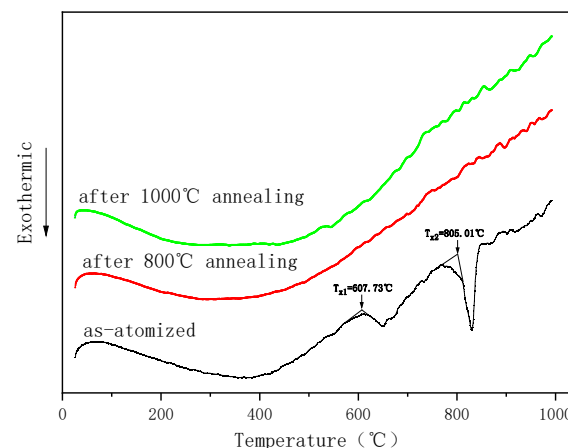

Figure 5. DSC curves of Fe-W-B amorphous powder as atomized and annealed.

Focused ion beam (FIB) sample image and EDS area microanalyses of as-atomized Fe-W-B amorphous powder are shown in Figure 6. EDS microanalyses show that the distribution of W and B elements are uniform within the Fe matrix, which conforms to the amorphous characteristic.

It can be seen from the XRD analysis that when the temperature reaches 700 °C, Fe-W-B amorphous powder begins to crystallize while the amorphous phase still exists. To further study the microstructure of Fe-W-B amorphous powder annealed at 700 °C, a TEM sample was prepared by FIB, as shown in Figure 7.
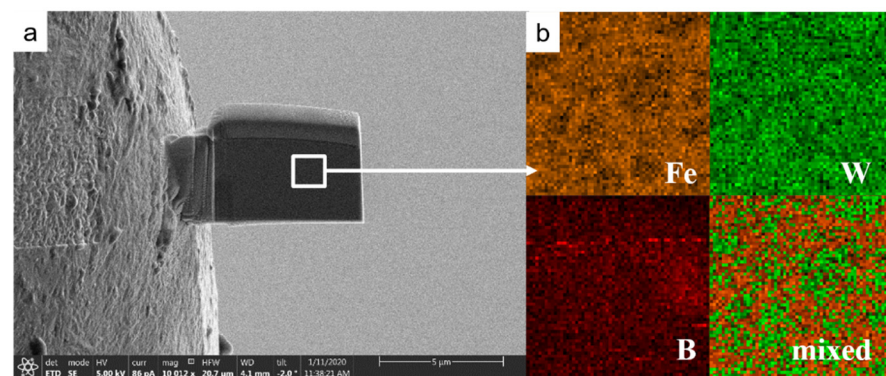
Figure 6. (**a**) FIB sample image and (**b**) EDS area microanalyses of as-atomized Fe-W-B amorphous powder.
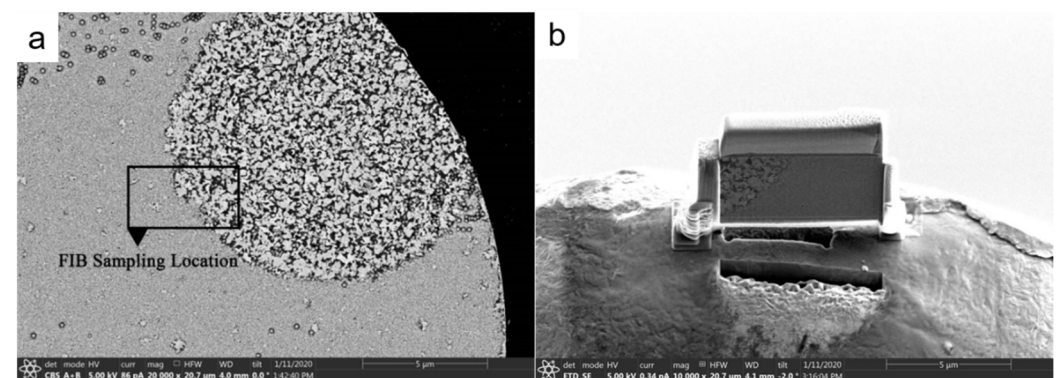

Figure 7. TEM sample image of Fe-W-B amorphous powder annealed at 700 °C. (**a**) FIB sampling location image; (**b**) FIB sample image.

The morphology and microstructure of Fe-W-B amorphous powder annealed at 700 °C are shown in Figure 8. Annealing induces crystallization. However, the crystallinity is inhomogeneous in the whole range of the particle. Crystallization occurs preferentially at the edge of the particle due to heat conduction. As shown in Figure 8a, the TEM sample can be divided into two regions, i.e., the amorphous-nanocrystalline dual phase region and the fully crystalline region. The microstructure morphology of the amorphous-nanocrystalline dual phase region is shown in Figure 8b. The SAED pattern of the amorphous-nanocrystalline dual phase region is shown in Figure 8c. The precipitated α-Fe nanocrystals are obvious. The corresponding SAED pattern shows {1 1 0}, {2 0 0}, {2 1 1}, {3 1 0}, {2 2 2} and {3 2 1} planes of α-Fe nanocrystals. Thus, the α-Fe phase should be precipitated before other compounds during crystallization annealing.

The microstructure morphology and EDS microanalyses of the fully crystallized region in Figure 8a is shown in Figures 8d and 8e, respectively. It can be seen from the HAADF image that there is a dendrite structure in the fully crystallized region. EDS microanalyses show that the bright phase corresponds to the tungsten enrichment area, and the dark phase corresponds to the iron enrichment area. Combined with XRD analysis results, it is expected that α-Fe and the compounds (i.e., Fe_7W_6 and FeWB) should be precipitated.

The HRTEM morphology of the fully crystallized region in Figure 8a is shown in Figure 8f. The SAED patterns of marked areas labeled with "SAED 1", "SAED 2" and "SAED 3" within the fully crystallized region are displayed in Figures 8g, 8h and 8i, respectively. The three SAED patterns correspond to three types of single crystals. The calibration of the three SAED patterns indicates the precipitates of α-Fe, FeWB and Fe_7W_6, respectively.
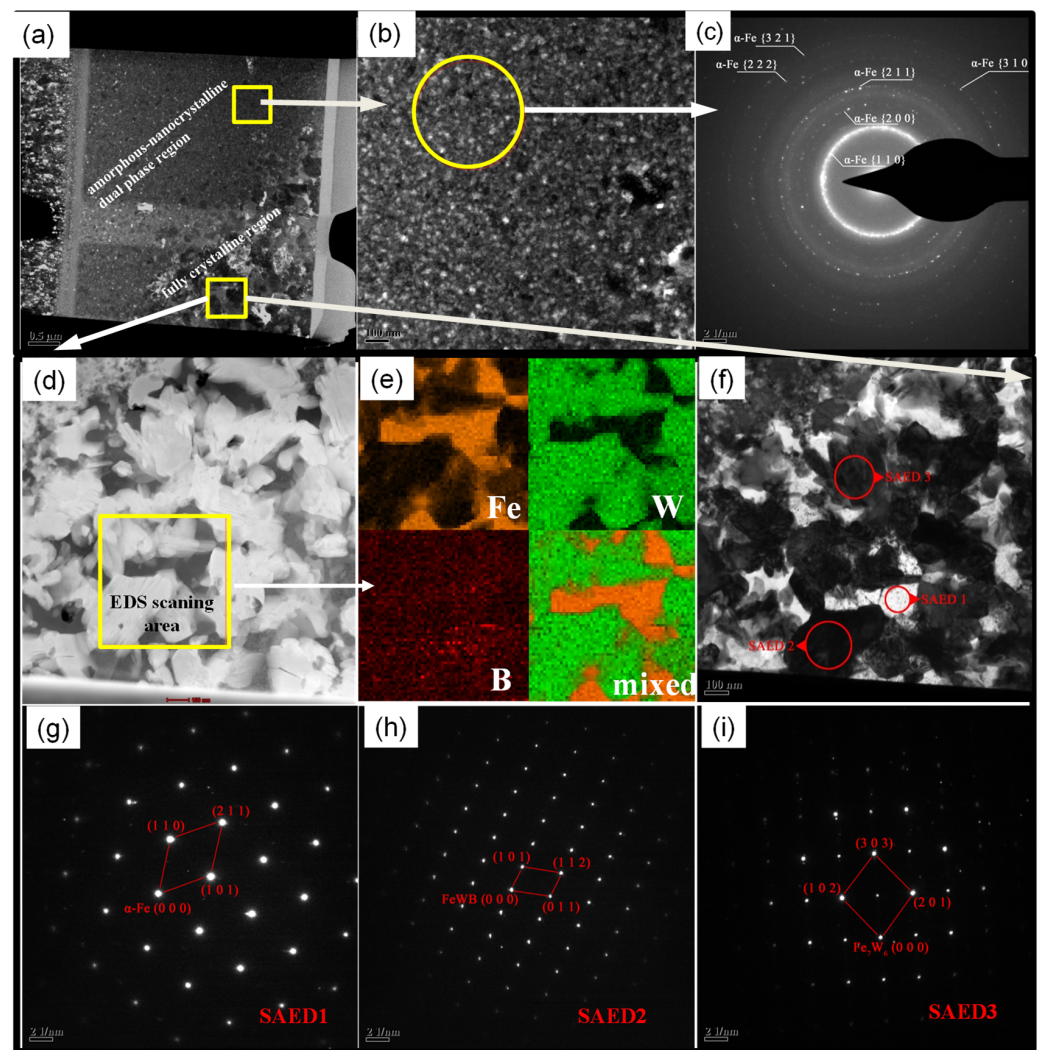
Figure 8. Microstructure of Fe-W-B amorphous powder annealed at 700 °C (TEM). (**a**) TEM sample image; (**b**) Microstructure morphology of the amorphous-nanocrystalline dual phase region; (**c**) SAED pattern of the amorphous-nanocrystalline dual phase region; (**d**) HAADF image of the fully crystallized region; (**e**) EDS microanalyses of the fully crystallized region; (**f**) HRTEM morphology of the fully crystallized region; (**g**) SAED pattern of "SAED1" within the fully crystallized region; (**h**) SAED pattern of "SAED2" within the fully crystallized region; (**i**) SAED pattern of "SAED3" within the fully crystallized region.

3.3. Nuclear Shielding Performance

Fe-W-B amorphous powder with high W and B contents should have good γ-ray and neutron shielding performance [31–35].

When the fluence rate of the γ-ray decays to half of the incident value, the corresponding medium thickness is called half attenuation thickness, which is often expressed by the symbol $d_{1/2}$, given as follows:

$$d_{1/2} = \frac{\ln 2}{\mu_l} = \frac{\ln 2}{\mu_m \cdot \rho_m} \tag{3}$$

where μ_l is the linear attenuation coefficient, μ_m is the mass attenuation coefficient, and ρ_m is the density of the shielding material.

The measured tap density of Fe-W-B amorphous powder is 7.2 g/cm^3, which was used in the calculation of γ-ray and neutron shielding performance. The corresponding density of iron is 7.8 g/cm^3.

Figure 9 shows the comparison of half attenuation thickness of Fe-W-B amorphous powder and iron under different γ-ray energy conditions. The smaller the half attenuation thickness, the better the shielding performance of the material to γ-rays. It can be seen from the figure that the half attenuation thickness of Fe-W-B amorphous powder is smaller than that of iron in the range of 0.1MeV~1.0MeV. In the range of 1MeV~5MeV, the half attenuation thickness of Fe-W-B amorphous powder is close to that of iron. When the γ-ray energy is greater than 5MeV, the half attenuation thickness of Fe-W-B amorphous powder is smaller than that of iron again. This is mainly because when interacting with γ-ray, tungsten has a better photoelectric effect than iron at lower energy and a better electron pair effect at higher energy, respectively.
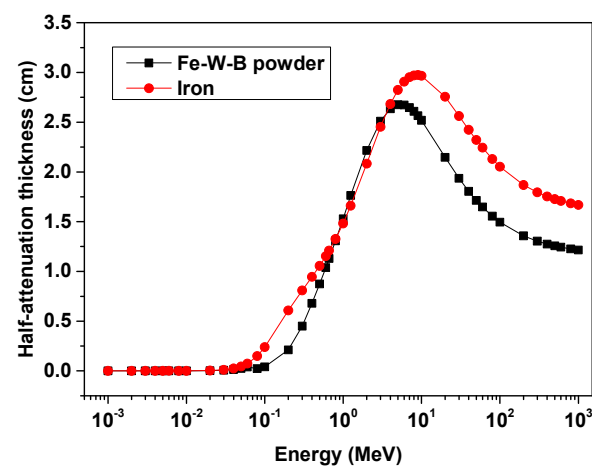

Figure 9. The comparison of half attenuation thickness of Fe-W-B amorphous powder and iron under different γ-ray energy conditions.

The neutron shielding properties of Fe-W-B amorphous powder and iron with a thickness of 30 cm to Cf-252 source neutrons are calculated by the Monte Carlo N Particle Transport Code (MCNP) program, as shown in Figure 10. The corresponding calculations are also carried out when there is no shielding material.
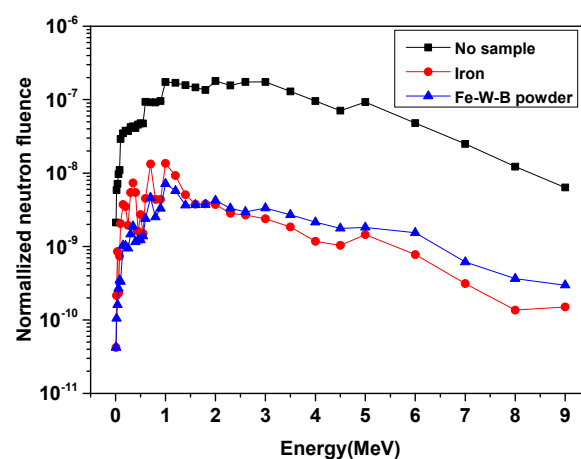

Figure 10. Neutron energy spectrum of Cf-252 source neutrons passing through Fe-W-B amorphous powder, iron and sample-free.

Neutron shielding performance can be quantified by neutron fluence attenuation ratio, which is calculated according to the following formula:

$$F_\Phi(E_n) = \Phi_0/\Phi_1 \tag{4}$$

where $F_\Phi(E_n)$ is the fluence attenuation ratio of the sample to neutrons with energy E_n, Φ_0 is neutron fluence at the detection point in the non-attenuated free field, and Φ_1 is neutron fluence at the detection point in the radiation field attenuated by sample.

According to the simulation results, the fluence attenuation ratio of Fe-W-B amorphous powder to Cf-252 source neutron is 37.0 and that of iron is 23.5. Meanwhile, the weight of Fe-W-B amorphous powder is lighter than that of iron at the same thickness. Therefore, compared with iron, Fe-W-B amorphous powder has better shielding performance for Cf-252 source neutrons.

Fe-W-B amorphous powder was loaded into an aluminum container with a thickness of 3 mm to prepare a testing sample for γ-ray and thermal neutron shielding performance. The test thickness of Fe-W-B amorphous powder is 10 mm and its tap density is 7.2 g/cm^3. The test results show that the attenuation ratios of the testing sample to ^{137}Cs γ-ray (662 kev) and ^{60}Co γ-ray (1250 kev) are 2.34 and 1.70, respectively. The absorption rate of the testing sample to thermal neutron is 98.5%.

4. Conclusions

In this study, Fe-W-B powders of various compositions were fabricated by gas atomization at 1700 °C. Fe-W-B amorphous powder was obtained with a high content of W and B under the high cooling rate of the gas atomization. The conclusions are summarized as follows:

1. Whether the atomized powder was crystalline or non-crystalline depends on the specific composition of the master alloy. Fe-W-B amorphous powder was formed under the master alloy composition of tungsten 19.9 at.%, boron 13.6 at.% and iron 66.4 at.%.
2. The structure of Fe-W-B amorphous powder is stable, which remains even as the temperature reaches 600 °C. After annealing at 700 °C, crystallization occurs preferentially at the edge of the particle. The precipitates in crystallization were α-Fe, FeWB and Fe$_7$W$_6$, respectively.
3. Compared with iron, Fe-W-B amorphous powder has better shielding performance for γ-rays and neutrons.

Author Contributions: Investigation and writing-original draft preparation, S.M.; Investigation and data curation, Z.L. and J.W.; Data curation, H.W.; Supervision and project administration, J.Y. and Z.Y.; Formal analysis, J.L. and Z.X. All authors have read and agreed to the published version of the manuscript.

Institutional Review Board Statement: Not applicable.

Informed Consent Statement: Not applicable.

Data Availability Statement: Data sharing is not applicable.

References

1. Li, C.; Yang, G.P.; Liu, Y.; Qiu, Y.C.; Li, J. A novel route of synthesising Fe–W–B alloy powders and characterisation thereof. *Powder Metall.* **2017**, *60*, 241–248. [CrossRef]
2. Klein, P.; Varga, R.; Kammouni, E.L.R.; Vazquez, M. Magnetic Properties of Glass-Coated FeWB Microwires. *Acta Phys. Pol.* **2014**, *126*, 70–71. [CrossRef]
3. Yang, G.P.; Li, J. Research on Microstructure and Properties of Fe-W-B Coatings Prepared by Plasma Spraying. *Guangzhou Chem. Ind.* **2016**, *44*, 143–145.
4. Li, C.; Li, J.; Liu, Y. Phase evolution of Fe–W–B powders and stability of FeWB ternary boride prepared by reactive synthesis. *Mater. Res. Express* **2018**, *5*, 016517. [CrossRef]
5. Li, J.L.; Li, J.; Li, C.; Liu, Y. Reactive synthesis of FeWB powders and preparation of bulk materials. *Int. J. Refract. Met. Hard Mater.* **2014**, *46*, 80–83. [CrossRef]

6. Li, C.; Li, J.L.; Li, J.; Liu, Y. Study on the synthesis behavior of Fe–W–B powders and the preparation of bulk. *Adv. Powder Technol.* **2015**, *26*, 1410–1416. [CrossRef]

7. Hang, Y.X.; Schwen, D.; Zhang, Y.F.; Bai, X.M. Effects of oversized tungsten on the primary damage behavior in Fe-W alloys. *J. Alloys Compd.* **2019**, *794*, 482–490.

8. Wang, Q.; Du, G.P.; Chen, N.; Jiang, C.S. First-principles study of bubble formation and cohesion properties of hydrogen at Fe/W interfaces. *Int. J. Hydrog. Energy* **2019**, *44*, 26469–26476. [CrossRef]

9. Azakli, Y.; Tarakci, M. Microstructural characterisation of borided binary Fe–W alloys. *Surf. Eng.* **2018**, *34*, 226–234. [CrossRef]

10. Wei, X.; Chen, Z.; Zhong, Z.; Wang, L.; Yang, W.; Wang, Y. Effect of alloying elements on mechanical, electronic and magnetic properties of Fe_2B by first-principles investigations. *Comput. Mater. Sci.* **2018**, *147*, 322–330. [CrossRef]

11. Tarek, B.; Rakia, D.; Lusia, E.; Joan, J.S.; Mohamed, K. Amorphization of $Al_{50}(Fe_2B)_{30}Nb_{20}$ mixture by mechanical alloying. *Metall. Mater. Trans. A* **2013**, *44*, 4718–4724.

12. Kirkovska, I.; Homolová, V.; Petryshynets, I.; Csanádi, T. The influence of the third element on nano-mechanical properties of iron borides FeB and Fe_2B formed in Fe-B-X (X = C, Cr, Mn, V, W, Mn + V) alloys. *Materials* **2020**, *13*, 4155. [CrossRef] [PubMed]

13. Takahashi, M.; Koshimura, M.; Abuzuka, T. Phase Diagram of Amorphous and Crystallized Fe-B Alloy System. *Jpn. J. Appl. Phys.* **1981**, *20*, 1821–1832. [CrossRef]

14. Chang, L.; Zhang, Y.Q.; Dong, Y.Q.; Li, Q.; He, A.N.; Chang, C.T.; Wang, X.M. Enhanced magnetic properties of Fe-based nanocrystalline composites by addition of carbonyl iron powders. *SN Appl. Sci.* **2019**, *1*, 902. [CrossRef]

15. Alvarez, K.L.; Martín, J.M.; Patov, M.; Gonzalez, J. Soft magnetic amorphous alloys (Fe-rich) obtained by gas atomisation technique. *J. Alloys Compd.* **2018**, *735*, 2646–2652. [CrossRef]

16. Gheiratmand, T.; Hosseini, H.M. Finemet nanocrystalline soft magnetic alloy: Investigation of glass forming ability, crystallization mechanism, production techniques, magnetic softness and the effect of replacing the main constituents by other elements. *J. Magn. Magn. Mater.* **2016**, *408*, 177–192. [CrossRef]

17. Ge, Y.; Ying, G.; Bangwei, Z.; Lingling, W.; Yifang, O.; Shuzhi, L. Preparation and thermal properties of amorphous Fe-W-B alloy nano-powders. *J. Mater. Process. Technol.* **1998**, *74*, 10–13. [CrossRef]

18. Zhao, X.M.; Xu, J.; Zhu, X.X.; Zhang, S.M.; Zhao, W.D.; Yuan, G.L. Characterization of 17-4PH stainless steel powders produced by supersonic gas atomization. *Int. J. Miner. Metall. Mater.* **2012**, *19*, 83–88. [CrossRef]

19. Zhao, X.M.; Xu, J.; Zhu, X.X.; Zhang, S.M. Effect of atomization gas pressure variation on gas flow field in supersonic gas atomization. *Sci. China* **2009**, *52*, 3046–3053. [CrossRef]

20. Zhao, X.M.; Xu, J.; Zhu, X.X.; Zhang, S.M. Effect of closed-couple gas atomization pressure on the performances of Al-20Sn-1Cu powders. *Rare Met.* **2008**, *27*, 439–443. [CrossRef]

21. Alvarez, K.L.; Martín, J.M.; Burgos, N.; Ipatov, M.; Domínguez, L.; González, J. Structural and magnetic properties of amorphous and nanocrystalline Fe-Si-B-P-Nb-Cu alloys produced by gas atomization. *J. Alloys Compd.* **2019**, *810*, 151754. [CrossRef]

22. Chang, L.; Xie, L.; Liu, M. Novel Fe-based nanocrystalline powder cores with excellent magnetic properties produced using gas-atomized powder. *J. Magn. Magn. Mater.* **2018**, *452*, 442–446. [CrossRef]

23. Chang, C.; Dong, Y.; Liu, M.; Guo, H.; Xiao, Q.; Zhang, Y. Low core loss combined with high permeability for Fe-based amorphous powder cores produced by gas atomization powders. *J. Alloys Compd.* **2018**, *766*, 959–963. [CrossRef]

24. Dong, Y.; Li, Z.; Liu, M.; Chang, C.; Li, F.; Wang, X. The effects of field annealing on the magnetic properties of FeSiB amorphous powder cores. *Mater. Res. Bull.* **2017**, *96*, 160–163. [CrossRef]

25. Wang, W.H. The nature and properties of amorphous matter. *Prog. Phys.* **2013**, *33*, 177–351.

26. Guo, J.J.; Fu, H.Z. *Alloy Melt and Treatment*; China Machine Press: Beijing, China, 2005; pp. 35–36.

27. Lashgari, H.R.; Chu, D.; Xie, S.S.; Sun, H.D.; Ferry, M.; Li, S. Composition dependence of the microstructure and soft magnetic properties of Fe-based amorphous/nanocrystalline alloys: A review study. *J. Non-Cryst. Solids* **2014**, *391*, 61–82. [CrossRef]

28. Lu, Z.P.; Liu, C.T. A new glass-forming ability criterion for bulk metallic glasses. *Acta Mater.* **2002**, *50*, 3501–3512. [CrossRef]

29. Öztürk, P.; Hitit, A. Effects of Tungsten and Boron Contents on Crystallization Temperature and Microhardness of Tungsten Based Metallic Glasses. *Acta Metall. Sin. (Engl. Lett.)* **2015**, *28*, 733–738. [CrossRef]

30. Ouyang, X.M.; Yin, F.C.; Hu, J.X.; Zhao, M.X. Experimental investigation and thermodynamic calculation of the B-Fe-W ternary system. *Calphad* **2018**, *63*, 212–219. [CrossRef]

31. Marshall, J.M.; Walker, D.; Thomas, P.A. HRXRD study of the theoretical densities of novel reactive sintered boride candidate neutron shielding materials. *Nucl. Mater. Energy* **2020**, *22*, 100732. [CrossRef]

32. Dewen, T.; Shuliang, Z.; Liang, Y. Influence of boron contents on microstructure, mechanical properties and shielding effect of Fe–W–C alloy. *J. Alloys Compd.* **2019**, *803*, 466–475. [CrossRef]

33. Zhao, S.; Huo, Z.; Zhong, G.; Zhang, H.; Hu, L. Research Progress of Neutron and Gamma-ray Composite Shielding Materials. *J. Funct. Mater.* **2021**, *52*, 03001–03015.

34. Wang, J.; Zou, S.L. Comparative Study of Tungsten and Lead as Gamma Ray Shielding Material. *J. Univ. South China (Sci. Technol.)* **2011**, *25*, 19–22.

35. Abouhaswa, A.S.; Sayyed, M.I.; Altowyan, A.S.; Al-Hadeethi, Y.; Mahmoud, K.A. Evaluation of optical and gamma ray shielding features for tungsten-based bismuth borate glasses. *Opt. Mater.* **2020**, *106*, 109981. [CrossRef]